How to cite: *Angew. Chem. Int. Ed.* **2024**, *63*, e202403189
doi.org/10.1002/anie.202403189

Layered Cathode Materials

Probing Particle-Carbon/Binder Degradation Behavior in Fatigued Layered Cathode Materials through Machine Learning Aided Diffraction Tomography

Weibo Hua[+], Jinniu Chen[+], Dario Ferreira Sanchez, Björn Schwarz, Yang Yang, Anatoliy Senyshyn, Zhenguo Wu, Chong-Heng Shen, Michael Knapp, Helmut Ehrenberg, Sylvio Indris,* Xiaodong Guo,* and Xiaoping Ouyang*

Abstract: Understanding how reaction heterogeneity impacts cathode materials during Li-ion battery (LIB) electrochemical cycling is pivotal for unraveling their electrochemical performance. Yet, experimentally verifying these reactions has proven to be a challenge. To address this, we employed scanning μ-XRD computed tomography to scrutinize Ni-rich layered $LiNi_{0.6}Co_{0.2}Mn_{0.2}O_2$ (NCM622) and Li-rich layered $Li[Li_{0.2}Ni_{0.2}Mn_{0.6}]O_2$ (LLNMO). By harnessing machine learning (ML) techniques, we scrutinized an extensive dataset of μ-XRD patterns, about 100,000 patterns per slice, to unveil the spatial distribution of crystalline structure and microstrain. Our experimental findings unequivocally reveal the distinct behavior of these materials. NCM622 exhibits structural degradation and lattice strain intricately linked to the size of secondary particles. Smaller particles and the surface of larger particles in contact with the carbon/binder matrix experience intensified structural fatigue after long-term cycling. Conversely, both the surface and bulk of LLNMO particles endure severe strain-induced structural degradation during high-voltage cycling, resulting in significant voltage decay and capacity fade. This work holds the potential to fine-tune the microstructure of advanced layered materials and manipulate composite electrode construction in order to enhance the performance of LIBs and beyond.

Introduction

In recent years, Li-ion batteries (LIBs) have sparked a revolution in the realm of portable electronics, driving the advancement of electric vehicles (EVs), facilitating the integration of renewable energy sources, and providing reliable portable power solutions across diverse industries.[1–5] The composite positive electrode used in LIBs consists of numerous electrochemically active crystallites embedded within a conductive carbon and binder matrix.[6,7] The microstructure of the composite cathode plays a crucial role in determining the performance of LIBs by influencing electronic and ionic transport properties, as well as chemical-mechanical behaviors.[8–10] Extensive research efforts have been dedicated to investigating the fatigue behaviors of active cathode materials,[11–13] including particle cracks,[14,15] disintegration,[16,17] and (de)activation.[18,19] Unfortunately, a limited number of studies have thoroughly clarified the structural degradation of cathode materials when interacting with a carbon/binder matrix due to the inherent challenge in

[*] Dr. W. Hua[+], J. Chen[+]
School of Chemical Engineering and Technology, Xi'an Jiaotong University, No.28, West Xianning Road, Xi'an, Shaanxi 710049, China
E-mail: weibo.hua@xjtu.edu.cn

Dr. W. Hua,[+] Z. Wu, Dr. X. Guo
School of Chemical Engineering, Sichuan University, No. 24 South Section 1, Yihuan Road, 610065, Chengdu, China
E-mail: xiaodong2009@scu.edu.cn

Dr. W. Hua,[+] B. Schwarz, M. Knapp, H. Ehrenberg, Dr. S. Indris
Institute for Applied Materials (IAM), Karlsruhe Institute of Technology (KIT), Hermann-von-Helmholtz-Platz 1, D-76344 Eggenstein-Leopoldshafen, Germany
E-mail: sylvio.indris@kit.edu

D. Ferreira Sanchez
Swiss Light Source, Paul Scherrer Institut (PSI), Forschungsstrasse 111, Villigen 5232, Switzerland

Y. Yang
National Synchrotron Light Source II (NSLS-II), Brookhaven National Laboratory, Upton, NY, 11973 USA

A. Senyshyn
Heinz Maier-Leibnitz Zentrum, Technische Universität München, Lichtenbergstrasse 1, D-85747 Garching, Germany

C.-H. Shen
Contemporary Amperex Technology Co., Ningde, 352100 China

X. Ouyang
School of Materials Science and Engineering, Xiangtan University, Xiangtan 411105, China

[+] These authors contributed equally to this work.

acquiring the spatial distribution of particle and carbon/binder phases.[20–22]

Indeed, the significance of fatigue behaviors occurring at the interphase between the cathode material and the conductive agent, as well as within relatively small particles, becomes apparent when considering the release or reception of electrons from the cathode materials and their traversal through the carbon conductive network.[23,24] Previous research has indicated the presence of local heterogeneity within the electrode,[4,25–27] including variations in individual particle reaction kinetics[28,29] and the uneven distribution of transition-metal (TM) ions in terms of their chemical composition and valence state.[3,30–32] Nowadays, synchrotron-based X-ray tomography is widely adopted to achieve precise, reliable, and efficient visualization of composite electrodes. This method enables three-dimensional imaging of electrode materials at both the electrode[33,34] and particle levels[35,36] under operating conditions. The combination of synchrotron-based transmission X-ray microscopy (TXM) and X-ray absorption near-edge structure (XANES) imaging[37,38] offers crucial insights into the local chemistry of LIBs. For instance, Jiang et al.[39] effectively utilized a combination of TXM and phase contrast tomography, augmented by machine learning, to visualize the evolution and gain insight into the electrochemical interactions between battery particles and the conductive matrix. However, relying solely on the TXM method limits the analysis to morphological features of the materials, without the ability to further examine local phase variations.[40–42] Although Transmission Electron Microscopy (TEM) is proficient in probing the crystallographic structure of cathode materials, its limited field of view restricts observation to very thin regions of the sample. Moreover, the interaction of high-energy electron beams with samples can induce electron beam radiation damage, leading to the destruction of sample structure.[43]

Recently, there has been a deployment of micro-focused beam scanning X-ray diffraction (μ-XRD) computed tomography (CT) to delve into the structural heterogeneity within electrode materials during operation.[38,44] However, such experiments, which involve extended periods of maintaining a specific voltage (not representative of real operational conditions) and necessitate spatially resolved X-ray diffraction signals, are time-consuming due to the need for sample rotation during raster scanning. μ-XRD CT typically yields a substantial amount of imaging data, with over 10,000 μ-XRD patterns per slice, posing challenges for traditional methods to handle effectively. Machine learning, on the other hand, offers a promising approach to efficiently identify and categorize specific structures within images. By swiftly and accurately pinpointing valuable areas, machine learning facilitates the extraction of meaningful features from complex datasets, enhancing our ability to comprehend, articulate, and streamline crucial information within imaging data. Additionally, prior research has indicated minimal changes in both the crystallographic structure and electrochemical capacity of electrode materials after just a single cycle.[11,13,45] Hence, delving into the structural heterogeneity of fatigued composite electrodes after prolonged cycling holds more significance.

Herein, the high sensitivity and high spatial resolution of X-ray diffraction computed tomography (XRD-CT) is harnessed to investigate the localized structural degradation of two specific materials: Ni-rich layered $LiNi_{0.6}Co_{0.2}Mn_{0.2}O_2$ (NCM622) and Li-rich layered $Li[Li_{0.2}Ni_{0.2}Mn_{0.6}]O_2$ (LLNMO). The μ-XRD pattern allows for the reconstruction of the phase mapping of active particles and carbon/binder based on their distinct reflection positions. Reconstructing and visualizing the layered particles in conjunction with the carbon/binder allows for tracing the spatial heterogeneity of the local crystalline structure across the entirety of secondary particles. To ensure comprehensive statistical representation, a combination of unsupervised and supervised learning methods is employed to categorize the carbon/binder, layered, and spinel phases within a series of μ-XRD tomographic slices of powder materials. The statistical analysis, aided by machine learning, reveals that the degradation of NCM622 is significantly related to the size of secondary particles and whether they come into contact with carbon/binder. On the contrary, after 100 cycles, a pronounced increase in the unit-cell volume of the layered structure and significant microstrain are observed in both the surface and bulk of LLNMO. This severe structural fatigue leads to rapid voltage decay and capacity fade over extended cycling periods. Additionally, we addressed an intriguing question concerning an oxide with a layered/spinel/rock-salt-type heterostructure, specifically whether these three phases exist within a single particle or in different particles.

Results and Discussion

The experimental setup of simultaneous micro-focused x-ray diffraction (μ-XRD) and fluorescence (μ-XRF) measurements (tomography and 2D-raster scan) is shown schematically in Figure 1a and Supplementary Figure S1. Utilizing a Kirkpatrick-Baez (KB) mirror system, the incident pencil beam was precisely focused, resulting in a beam size of approximately 1.0×1.0 (H×V) μm^2. Micro-focused x-rays are directed onto a capillary with a diameter of 0.1 or 0.5 mm, which contains either as-synthesized oxide materials or mixed powders extracted from the electrode. The tomography experiments were carried out by recording simultaneously both the XRD 2D patterns and XRF spectra at selected positions in the x direction, in steps of 1 or 2 μm, and at 180 sample orientations equally spaced by a rotational angle of 1° (ω). The μ-XRD CT method primarily scrutinizes the active cathode materials and fatigue electrodes. It processes 2D diffraction images obtained at varied sample rotations (ω) and positions (x), converting them into one-dimensional (1D) diffraction patterns (Figures S2–S3). This conversion condenses the stack of images into a three-dimensional (3D) dataset, incorporating sample position (x), scattering angle (2θ), and tomographic angle (ω). Summing the linear 1D XRD patterns across x and ω ($N_x \times N_\theta$) yields a 1D sum pattern, facilitating the identification of main

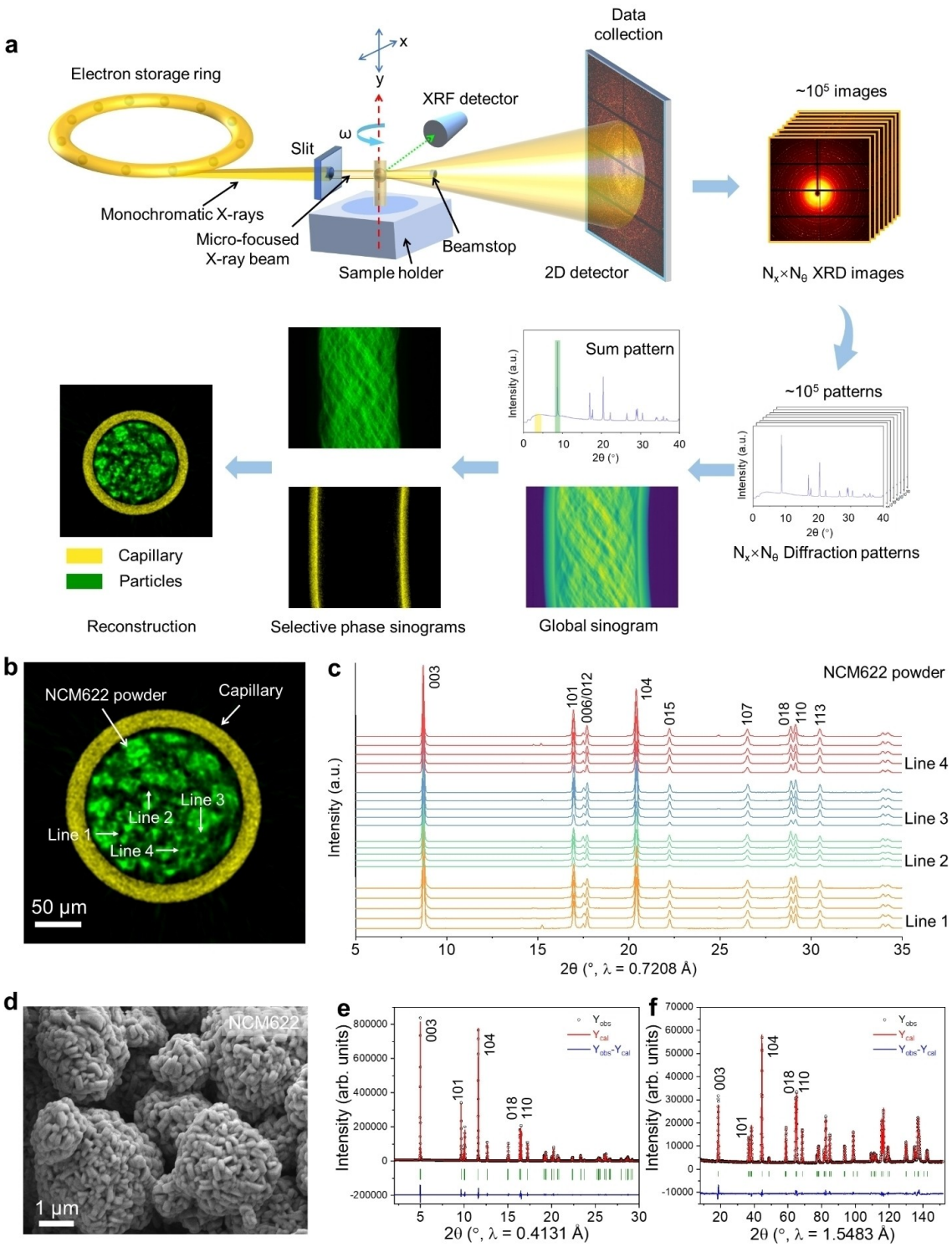

Figure 1. Microstructural analysis of pristine NCM622. **a** Schematic illustration of experimental setup at the microXAS beamline (Swiss Light Source, Paul Scherrer Institut) of synchrotron-based 2D and 3D μ-XRD and μ-XRF measurements. At each position (x, ω), the 2D diffraction pattern integrates across the scattering angle (2θ), producing the respective 1D XRD pattern, denoted as $f(2\theta)$. These individual 1D diffraction patterns are then aggregated across x and ω to form a scattering sum pattern for the entire sample. Simultaneously, each 1D $f(2\theta)$ pattern is integrated across the azimuthal angle, resulting in a total scattering intensity represented as a function of (x, ω), constructing the global sinogram. Specific sinograms for distinct phases, identified by a diffraction peak (green rectangular in sum pattern) or a particular scattering contribution (yellow rectangular), can be extracted. Consequently, a reconstruction comprising axial slices of the respective phases is generated using these sinograms. **b** The cross-sectional image delineates the spatial distribution of various phases: the spherical-like NCM622 particles are depicted in green, while the yellow ring represents the glass capillary. **c** Corresponding XRD patterns over these regions of interest (ROIs) in the Figure **b** unveil a consistent homogeneous layered phase within NCM622. **d** SEM image, and simultaneous Rietveld refinement against **e** SXRD ($\lambda = 0.4131$ Å) and **f** NPD ($\lambda = 1.5483$ Å) patterns of NCM622.

phases. Generating a cross-section of the whole diffraction involves creating a global sinogram via integrated 1D diffraction patterns across 2θ concerning x and ω. Alternatively, selecting a region of interest (ROI) or specific reflections on the 1D diffraction patterns can construct sinograms over particular 2θ ranges, depicted as green and yellow rectangles in sum pattern in Figure 1a. Each XRF or XRD intensity contributes to constructing sinograms, which are subsequently employed in a simultaneous iterative reconstruction technique (SIRT).[40] This particular method involves a reverse analysis using XRD sinograms for recovering local crystalline phases and XRF sinograms for determining local chemical compositions. Both signals furnish depth-resolved information in a two-dimensional manner. Thus, for every voxel (about 1 μm) associated with a specific 3D spatial sample position, both the local XRD pattern and the local XRF spectrum are derived. This approach enables comprehensive analysis of materials at a micro-scale level.

Figure 1b shows one reconstructed (x, y) slice of the as-prepared $LiNi_{0.6}Co_{0.2}Mn_{0.2}O_2$ powder (NCM622) derived from the sinograms of Figure 1a. The NCM622, highlighted in green and enclosed within a capillary outlined by a yellow ring, distinctly displays a spherical-like shape, consistent with the scanning electron microscopy (SEM) image in Figure 1d. Furthermore, SEM image illustrates that the NCM622 is composed of multiple small platelet-like crystalline grains that agglomerate into larger quasi-spherical secondary particles. The average size of secondary particles of NCM622 measured by light scattering is around 6 μm. The averaged XRD pattern of NCM622 over the entire 2D scanned area matches its synchrotron-based XRD (SXRD) pattern (see Supplementary Figure S4), confirming the reliability of the 2D μ-XRD data processing and analysis. The scanning μ-XRF images in Supplementary Figure S5 reveal a homogeneous distribution of Ni, Co, and Mn ions in NCM622. As shown in Figure 1c, the local XRD patterns of NCM622 across four distinct lines reveal that all reflections can be assigned to a single layered phase (space group $R\bar{3}m$). There are no detectable impurities or shifts in reflection, affirming the successful synthesis of pure layered NCM622. Simultaneous Rietveld refinement results against SXRD and neutron powder diffraction (NPD) patterns further confirm (Figure 1e and f) that the as-synthesized NCM622 possesses a single layered phase with the same space group of $R\bar{3}m$. Refinement results yield lattice parameters of $a = 2.8753(2)$ Å, $c = 14.2356(6)$ Å and unit-cell volume $V = 101.9250(9)$ Å^3, and a reliable structure model of $[Li_{0.95}Ni_{0.05}]_{oct}[Li_{0.05}Ni_{0.55}Co_{0.2}Mn_{0.2}]_{oct}O_2$ (the subscript "oct" denotes the octahedral sites), see Supporting Information Table S1. Hard X-ray absorption spectroscopy (XAS) was utilized to trace the bulk oxidation states of TM ions in NCM622. X-ray absorption near edge structure (XANES) region of XAS spectra (Supplementary Figure S6) show that oxidation states of Ni, Co and Mn are predominately assigned to $Ni^{2.6+}$, Co^{3+} and Mn^{4+}, respectively, consistent with an average oxidation state of 3+ for the transition metals.

To elucidate the correlation between crystallographic structure and electrochemical property, the prepared NCM622 was fabricated into a CR2032-type coin cell for assessing its electrochemical performance. The NCM622/Li cells were galvanostatically cycled at 0.1 C (28 mA g^{-1}) between 2.7 and 4.3 V at room temperature (see Figure S7). Figure 2a exhibits the cyclic performance and the corresponding charge/discharge voltage profiles of NCM622. The initial discharge capacity of NCM622 at 0.1 C is approximately 178 mAh g^{-1}. After 100 cycles, the specific discharge capacity of NCM622 decreases to about 154 mAh g^{-1}, with a capacity retention of 87 %, which is comparable to the reported value in the literature.[25,46] The contour profiles of the evolution of several main reflections in the *in situ* SXRD patterns of the NCM622 cathode during the first cycle are depicted in Figure S8a. The reflections sensitive to changes in the c-axis, such as 003 and 018, initially shift towards lower scattering angles and then move to higher angles during the charging process. Simultaneously, reflections associated with variations in the a-axis, such as 101 and 110, shift to higher 2θ angles. The continuous shift of all reflections reveals a solid solution reaction mechanism during the Li-ion extraction-insertion process. The lattice parameters of NCM622 obtained from Rietveld refinement are exhibited in Figure S8b. Upon de-lithiation, the lattice parameter a of NCM622 progressively decreases, while the parameter c initially increases and then declines dramatically. These changes in lattice parameters are quite similar to the previously reported results.[47,48] Notably, there is a minimal variance, less than 0.2 %, in the lattice parameters of NCM622 before and after the initial cycle. Therefore, it is crucial to delve into the structural fatigue of the NCM622 cathode after extended cycling.

Figure 2b displays the averaged μ-XRD pattern of fatigued NCM622 cathode after 100 cycles at 0.1 C in the discharged state. A noticeable shift to lower scattering angles in all reflections of the fatigued NCM622, compared to the pristine powder, suggests an expanded lattice parameter within its layered structure. Furthermore, the Full Width at Half Maximum (FWHM) of all reflections in the sum XRD pattern of the fatigued NCM622 appears broader, while the splitting of reflections in the 006/012 and 018/110 doublets is reduced. These findings might arise due to higher lattice disorder or distortion in the long-range range, rather than the diverse states of lithiation within individual particles, as evidenced by the absence of any reflection shift in the local μ-XRD pattern of the fatigued particles (visible below). Significantly, weak reflections linked to the carbon/binder phase (around 2.3°) and spinel phase (approximately 8.2°) are discernible in the cycled NCM622 cathode. These reflections are distinguishable from the layered oxides. Thus, these specific scattering angles can be utilized to determine the spatial distribution of layered phase, spinel phase and carbon/binder matrix. While the spinel phase frequently emerges in Ni-rich cathode materials after long-term cycling,[10,49,50] a pertinent question remains unanswered: where precisely is the spinel phase located within the cycled Ni-rich electrode?

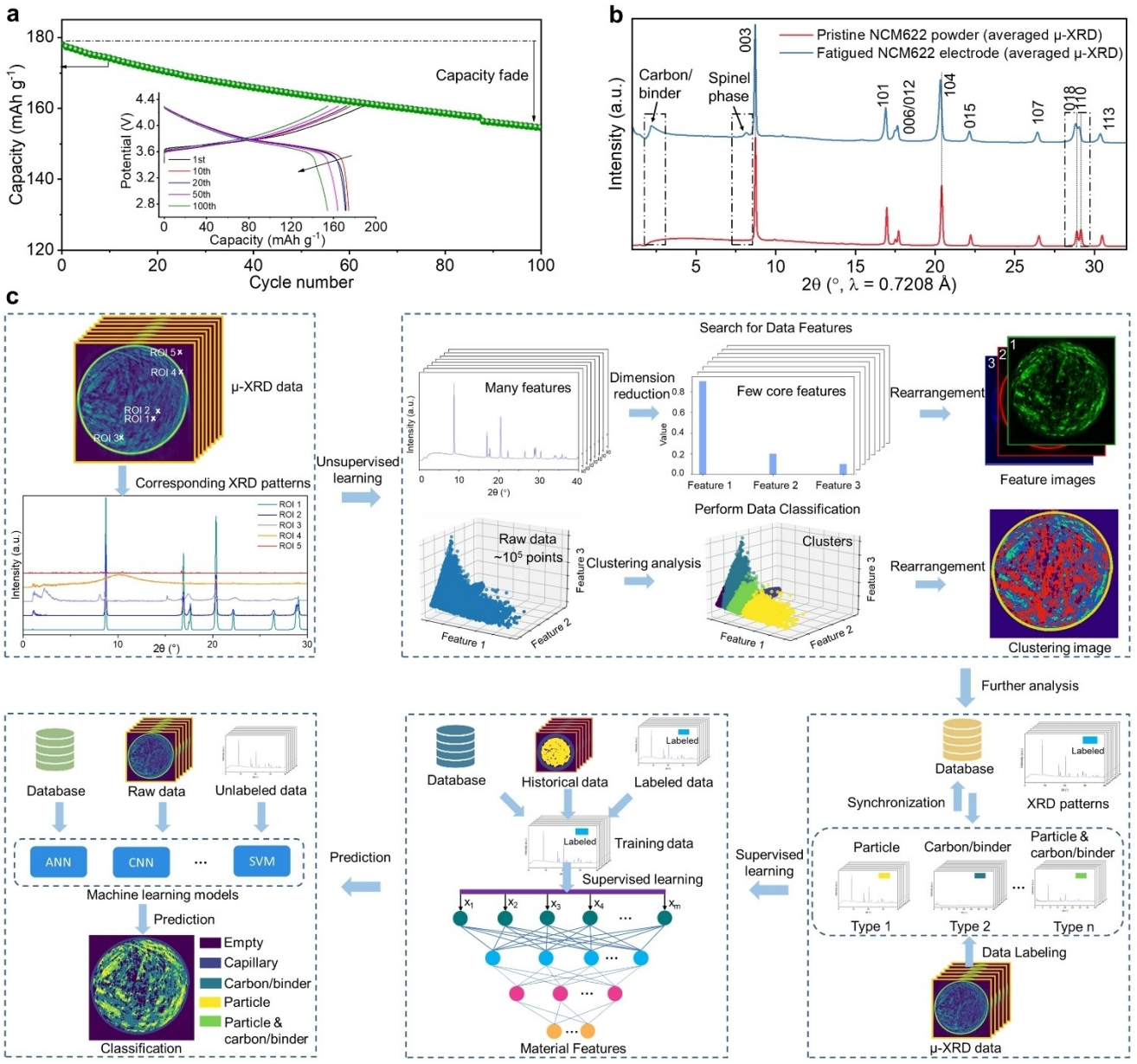

Figure 2. Machine-learning (ML)-assisted analysis of local structural degradation of the NCM622 cathode after long-term cycling. **a** Cycling performance of NCM622 electrode between 2.7 and 4.3 V at a current density of 0.1 C, inset is the corresponding charge–discharge voltage profiles. **b** Comparison of averaged μ-XRD patterns between pristine NCM622 powder (red curve) and fatigued NCM622 electrode in discharged state after over 100 cycles (blue curve), illustrating the presence of conductive carbon/binder matrix (broad reflection at approximately 2.3°) and spinel phase (a faint reflection at around 8.2°) in the cycled NCM622 electrode. **c** Schematic depiction of the data preprocessing approach employed for visualizing distinct spatial phase distributions from approximately 100,000 μ-XRD patterns, utilizing a combination of unsupervised and supervised learning methods.

Figure 2c illustrates how the local μ-XRD pattern reveals critical details about different components within fatigued electrode, including the cycled NCM622 particles, carbon/binder matrix, capillary, and empty regions. Analyzing a vast dataset of approximately 100,000 μ-XRD patterns involves a blend of unsupervised and supervised learning techniques. Details of classification and strain analysis are shown in Figures S9–S19. Initially, preparing the data involves cleaning and normalizing it for consistency. Dimensionality reduction techniques like Principal Component Analysis (PCA) condense the dataset to three core features. Unsupervised clustering algorithms such as k-means or density-based spatial clustering of applications with noise (DBSCAN) assist in identifying similar patterns, providing an initial view of spatially linked phase distributions. Subsequently, the XRD patterns are classified into five distinct categories—empty spaces, capillary, carbon/binder matrix, fatigued NCM622 particles, and particles with carbon/binder. To refine the precision of predicting spatial phase distributions, we meticulously labeled the dataset and

subsequently trained supervised models. The model's reliability is assessed through cross-validation. In light of the inherent variability in XRD patterns across different materials, the effectiveness of a singular machine learning approach cannot be universally guaranteed across all datasets. Consequently, to address this variability, we explore the application of four diverse machine learning methods: support vector machine (SVM), artificial neural network (ANN), k-nearest neighbor (KNN), and convolutional neural network (CNN). This ensemble learning aims to identify the most suitable model for the given dataset, ensuring a robust and adaptable solution. These methods showcase an accuracy exceeding 92 %, signifying their effectiveness in accurately classifying the spatial phase distribution of fatigued Ni-rich cathode materials.

To investigate the structural degradation and reaction heterogeneity of cycled NCM622 cathode, a tomographic scanning of three slices using μ-XRD technique was conducted. Figure 3a displays the resulting μ-XRD tomographic reconstructions for these slices. Analyzing the local distribution of various compounds in slice 1, i.e. carbon/binder & layered & spinel phases, was aided by machine-learning (ML) techniques, as depicted in Figures 3b, c, and e. Figure 3d present the corresponding reconstructed μ-XRD patterns of each voxel selected from surface to bulk of large secondary particles (line 1). Within the inner part of large agglomerates, all reflections are identifiable as a rhombohedral layered structure ($R\bar{3}m$). No reflection shift indicates consistent lattice parameters throughout the particle and a uniform state of lithiation. Notably, in the interphase between the larger particle and carbon/binder, new reflections attributed to a cubic spinel phase ($Fd\bar{3}m$), such as 111_S (subscript S denotes spinel phase) at around 8.2°, emerge. This transformation from a layered to a spinel phase confirms significant structural degradation specifically on the surface of the larger particle in contact with the carbon/binder. While the primary phase can be still attributed to the layered structure ($R\bar{3}m$) within smaller light blue spots wrapped by carbon/binder, the presence of the spinel phase is noticeable both on the surface and within the bulk of the particle. This evidence is illustrated in the μ-XRD patterns along line 2 in Figures 3e and f. These small spots in cross-sectional image are associated with either small particles or the surfaces of large agglomerates. Figure 1d clearly depicts small secondary particles with a diameter of 1–2 μm. Consequently, it can be interred that the degradation pathways of NCM622 particles are notably affected by the size of secondary particles and their interaction with the particle/carbon matrix.

To investigate the relationship between particle-carbon/binder interphase and local lattice strain in the NCM622 cathode material, the lattice strain (ε) of all NCM622 particles was estimated using the Williamson–Hall (W–H) method,[51,52] as described below:

$$\beta_{hkl}\cos\theta_{hkl} = \frac{K\lambda}{D} + 4\varepsilon \sin\theta_{hkl} \quad (1)$$

where β_{hkl} is the integral breadth of the *hkl* reflection corrected by instrumental contributions, K is shape factor (0.9), λ is wavelength, D is the volume weighted averaged crystallite size. The 2D maps of the local strain within both pristine NCM622 powder and cycled NCM622 particles are displayed in Figures 4a and b. The analysis clearly reveals an increased micro-strain in the cycled NCM622 particles, particularly in smaller particles, highlighted in yellow color. To accurately quantify the microstrain changes after prolonged cycling, we assessed lattice strain extracted from individual voxels or μ-XRD patterns, as depicted in Figures 4g–i. The average microstrain of NCM622 particles increased from 5.9×10^{-4} in their pristine state to approximately 7.9×10^{-4} after 100 cycles. Moreover, the observed increase to an average microstrain of 9.4×10^{-4} in cycled NCM622 particles interacting with carbon/binder reinforces the understanding that the surface area of active materials in contact with carbon/binder experiences more pronounced structural deterioration. Specifically, the surface-near regions of larger secondary particles show heightened lattice strain (depicted in light yellow in Figure 4e) compared to their inner regions (shown in dark blue). The presence of mixed spinel and layered phases in small light blue spots leads to a substantial lattice strain due to the layered-to-spinel phase transition, showcased in Figures 4b,c,e, and f. Even within smaller green spots displaying a single layered phase, their lattice strain surpasses that of larger agglomerates. Hence, these smaller spots are most likely associated with the small particles. These findings unveil a robust correlation between lattice strain and the size of secondary particles. Irrespective of whether smaller particles undergo a phase transition, their interaction with carbon/binder renders them more susceptible to encountering lattice strain and structural degradation.

Li- and Mn-rich layered oxides are considered promising cathode materials due to their high capacity and low cost.[53] However, they suffer from severe voltage decay over cycling, which hinders their practical application.[54] A typical Co-free Li-rich layered cathode material, i.e. Li-$[Li_{0.2}Ni_{0.2}Mn_{0.6}]O_2$ (LLNMO), was chosen to interpret the structural origin of voltage degradation (Supplementary Figures S20–S21 and Table S2). Clearly, it can initially deliver a discharge capacity of 252 mAh g^{-1} at 0.1 C within the voltage range of 2.0 to 4.8 V at room temperature, as shown in Figure 5a. During the initial 10 cycles, there is a rapid capacity fade from 252 to approximately 210 mAh g^{-1}, followed by a slight linear decrease with an increasing number of cycles. After 100 cycles, the discharge specific capacity of LLNMO is around 163 mAh g^{-1}, with a capacity retention of approximately 65 %. The corresponding charge–discharge voltage profiles of the LLNMO/Li cell indicates a significant voltage decay and capacity fade. These charge–discharge characteristics align well with the findings reported in the literature.[4,55,56]

To gain new insights into the origin of voltage fade in the LLNMO cathode material, μ-XRD tomography was employed. By comparing the averaged μ-XRD pattern of the pristine LLNMO powder with that of the LLNMO cathode after 100 cycles, a noticeable shift of all reflections

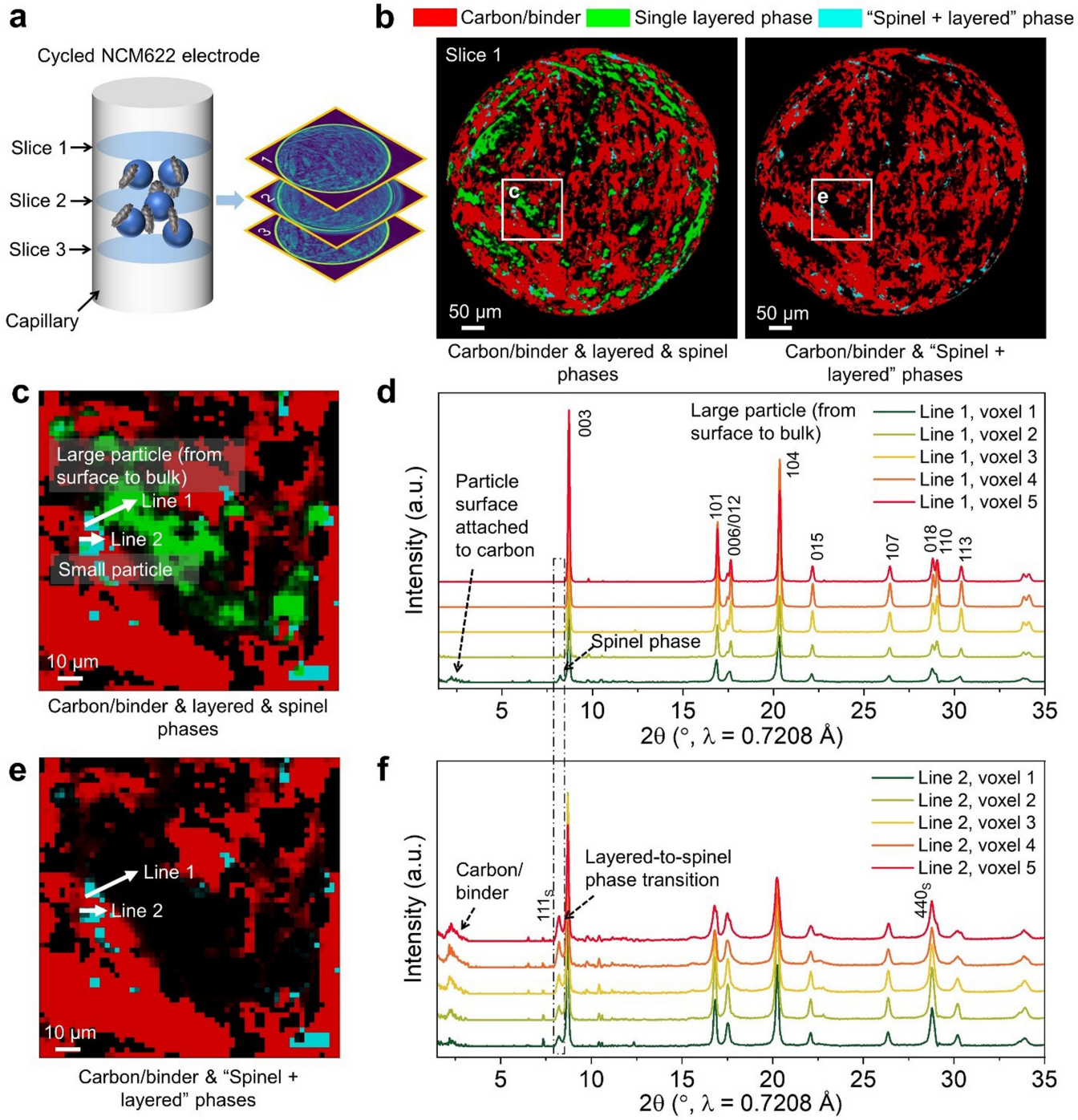

Figure 3. Visualization of the spatial phase distribution in the fatigued NCM622 cathode after 100 cycles at 0.1 C in the discharged state. **a** Illustrative μ-XRD scanning tomography diagram for three slices. **b** Cross-sectional view of local distribution of carbon/binder & layered & spinel phases in the cycled NCM622 cathode, the right figure emphasizes the predominant formation of spinel phase (light blue color) within small spots surrounded by carbon/binder matrix. Selected region of phase distributions with **c** single layered phase and **e** without single layered phase, and the corresponding μ-XRD patterns along **d** (line 1) and **f** (line 2) in figure **c**.

to lower 2θ angles is observed. This movement suggests a higher degree of long-range cationic disordering within the layered structure, transitioning from Li–O–[Li/TM] chains in the monoclinic layered structure to [Li/TM]–O–[Li/TM] linkages in the disordered structure.[9,10] After 100 cycles, the unit-cell volume of the layered structure expands to 208.35 Å^3, marking a significant increase from its initial 202.01 Å^3. In particular, the unit-cell volume of LLNMO increases by 3.13 %, surpassing that of NCM622, which only experiences a 1.26 % increase. The μ-XRD tomographic reconstructions for pristine LLNMO are displayed in Figure 5c and d. Figure 5e shows the local μ-XRD patterns

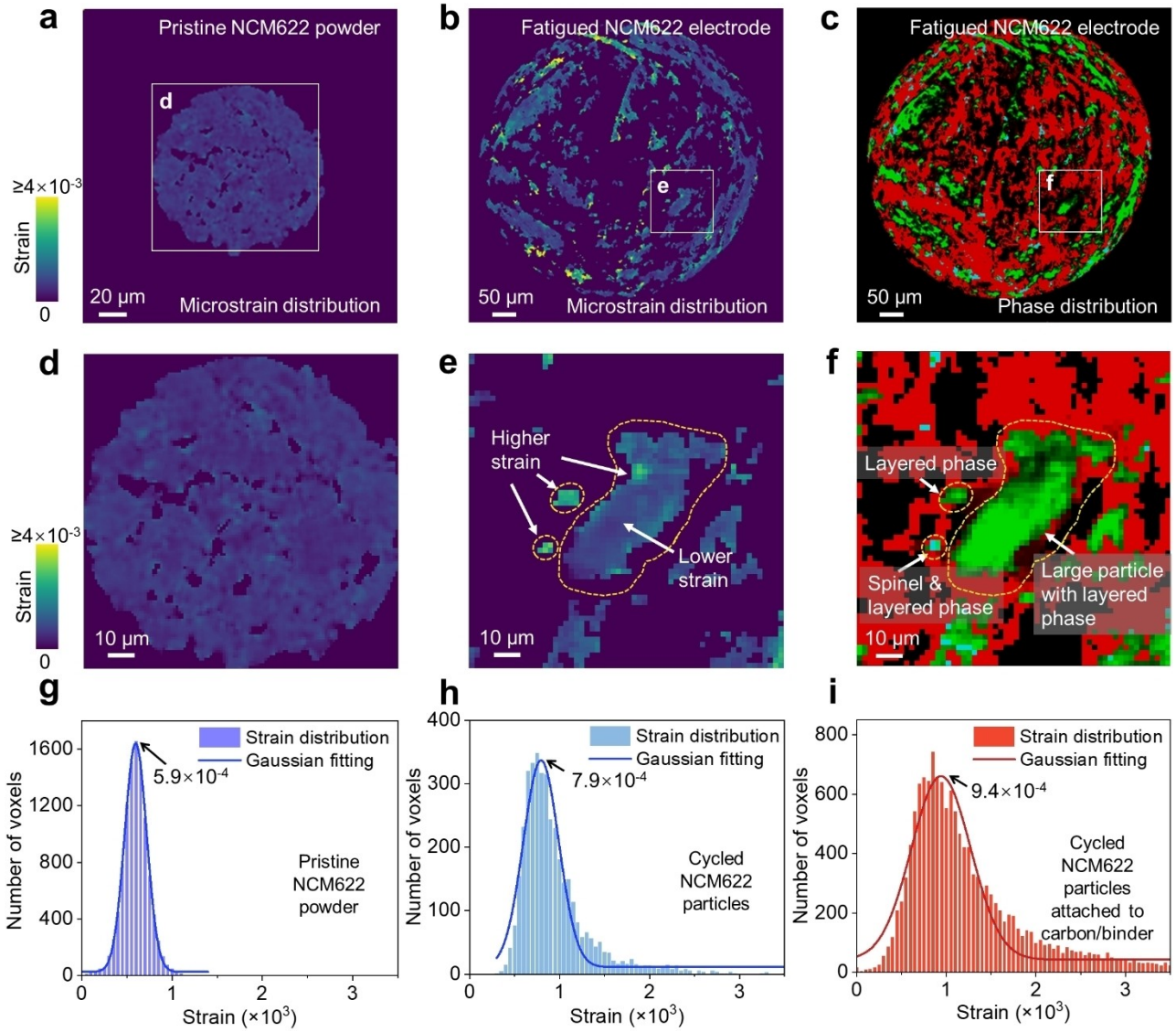

Figure 4. Intrinsic relationship between structural degradation and microstrain in fatigued NCM622 cathode after extended cycling (in the discharged state). **a**,**d** The 2D maps of local microstrain distribution of pristine NCM622 powder. **b**,**e** The microstrain distribution maps and **c**,**f** corresponding phase distribution maps of fatigued NCM622 cathode. Histograms for microstrain distribution and Gaussian fitting curve of **g** pristine NCM622 powder, **h** cycled NCM622 particles without contact with carbon/binder and **i** cycled NCM622 particles in contact with carbon/binder, revealing that the surface of cycled NCM622 particles attached to the high-conductivity carbon experiences more intense strain.

selected from various voxels. No shift or additional reflections are observed, suggesting that the prepared LLNMO consists of many layered crystallites with the same monoclinic structure (*C2/m*) and unchanged lattice parameters. After 100 cycles, the disappearance of superlattice reflections (e.g. 020) suggests the vanishing of Li/TM cation ordering in the TM layer of layered structure. While the surface and interior of fatigued LLNMO particles exhibit minimal change in reflection shifts, these reflections in the μ-XRD pattern consistently shift towards lower scattering angles compared to the original LLNMO powder. Analysis of the Ni and Mn K-edges XANES spectra reveals no discernible alteration in fatigued LLNMO compared to its pristine state (Figure S22), indicating that the oxidation state of Ni and Mn ions remains unchanged as Ni^{2+} and Mn^{4+}. Thereby, the observed reflection shifts suggest a uniform increase in long-range cationic disordering across the secondary particles. This disordering likely induces heightened lattice strain within the fatigued LLNMO particles, as depicted in Figures 5i and j. The average microstrain of LLNMO particles increases to approximately 1.0×10^{-3} after 100 cycles, up from 6.0×10^{-4} in the pristine powder (Figure 5k). Notably, there is no significant rise in microstrain observed in cycled LLNMO particles in contact with carbon/binder, contrasting with the degradation behavior observed in the NCM622 cathode. These findings highlight the transition from Li-rich monoclinic layered oxide to the Li-containing disordered layered phase as a crucial element influencing the voltage fade behavior in Li-rich layered

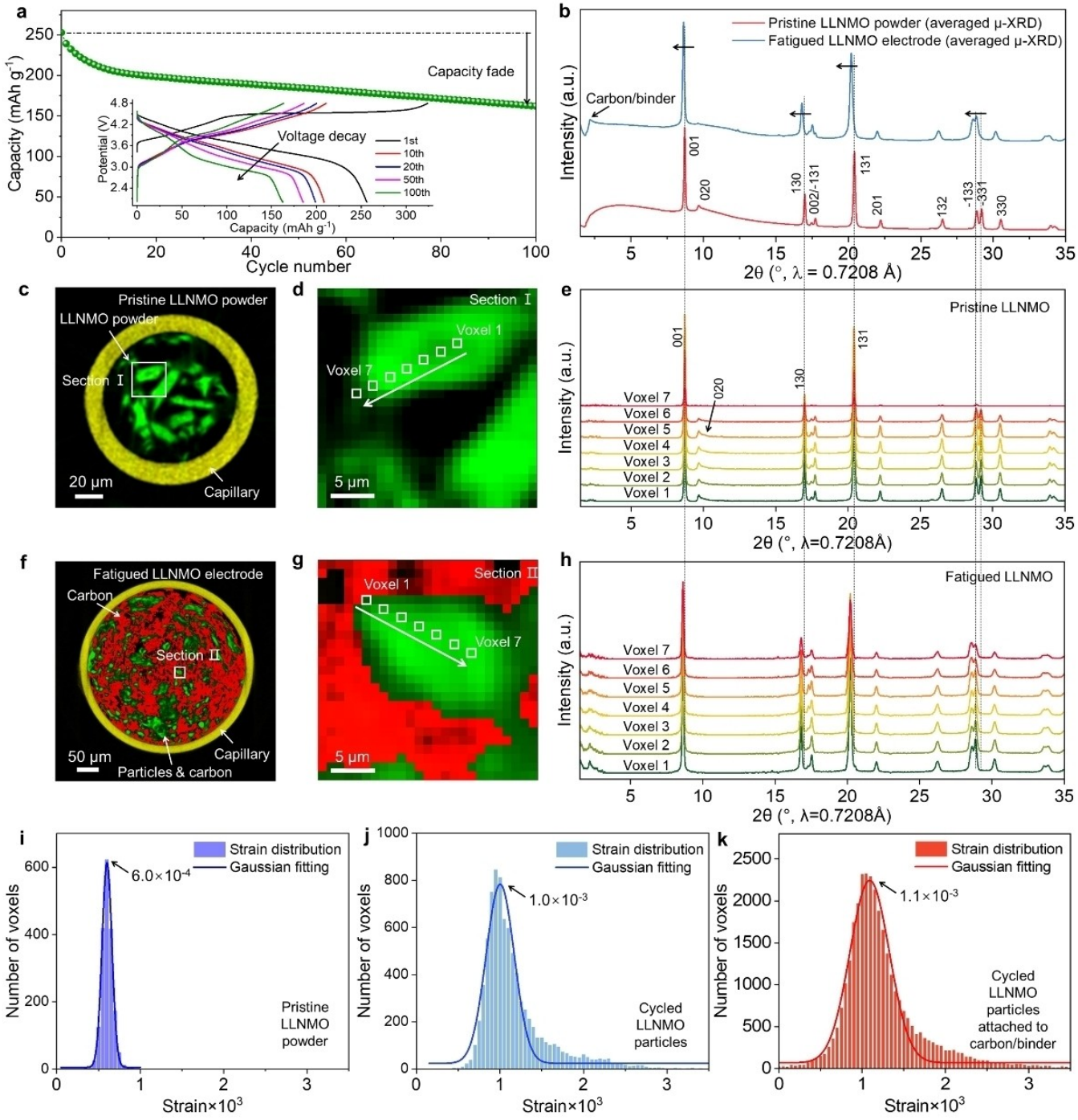

Figure 5. Structural degradation of the LLNMO cathode during high-voltage cycling. **a** Cyclic performance of LLNMO cathode within the voltage range of 2.0 to 4.8 V operating at a current density of 0.1 C, and the corresponding selected charge–discharge voltage curves (inset). **b** Averaged μ-XRD pattern over the whole 2D scanned area of pristine LLNMO powder (red curve) and cycled LLNMO electrode after 100 cycles (blue curve). Phase distribution maps of **c** fresh LLNMO powder and **f** fatigued LLNMO cathode. **d** Magnified view of the region highlighted in figure **c**; **e** local μ-XRD pattern corresponding to the various voxels in figure **d**. **g** Magnification of the region given in figure **f**, and **h** the corresponding local XRD patterns over the various voxels in **g**. Histograms for microstrain distribution and Gaussian fitting profile of **i** pristine LLNMO powder, **j** cycled LLNMO particles without contact with carbon/binder and **k** cycled LLNMO particles in contact with carbon/binder.

cathodes during long-term cycling, which aligns seamlessly with the conclusions drawn in the previous study.[9]

Discussion

On the basis of all results described above, it is found that the degradation pathways of Ni-rich oxide and Li-rich

cathode materials are different, although both oxides possess a similar layered structure. This is to say, Ni-rich NCM622 oxide experiences a transition from "Li-rich" layered phase to "Li-poor" spinel phase upon extended cycling at room temperature, while LLNMO cathode undergoes a transition from Li-rich ordered layered phase to Li-containing disordered layered phase, see Figure 6. Given the NCM622's retention of around 87 % capacity after 100 cycles between 2.7 and 4.3 V at 0.1 C, it's likely that capacity fade stems more from the structural fatigue of small particles under higher strain than from larger particles with lower strain. Considering μ-XRD's 3D spatial limit of 1 μm, the definition of small particles here includes secondary particle sizes below 3 μm and above 1 μm. The shorter Li-ion diffusion length in these small secondary particles makes them vulnerable to the layered-to-spinel phase transition, resulting in significant lattice strain and subsequent capacity fading. In the case of LLNMO, both surface and bulk crystallites experience strain-induced structural earthquake, leading to pronounced voltage decay and capacity loss during high-voltage cycling.

Additionally, the combination of μ-XRD and μ-XRF represents powerful tools for investigating the interaction between structure and chemical signatures in hetero-structured cathodes, providing a 3D spatial resolution of 1 μm. Addressing the spatial resolution of elemental distribution and its correlation with the crystalline phase in spinel/layered/rock-salt heterostructured materials has been a long-standing concern for scientists.[57] To address this question, we successfully synthesized a "$Li_{0.9}Ni_{0.2}Mn_{0.6}O_{1.9}$"

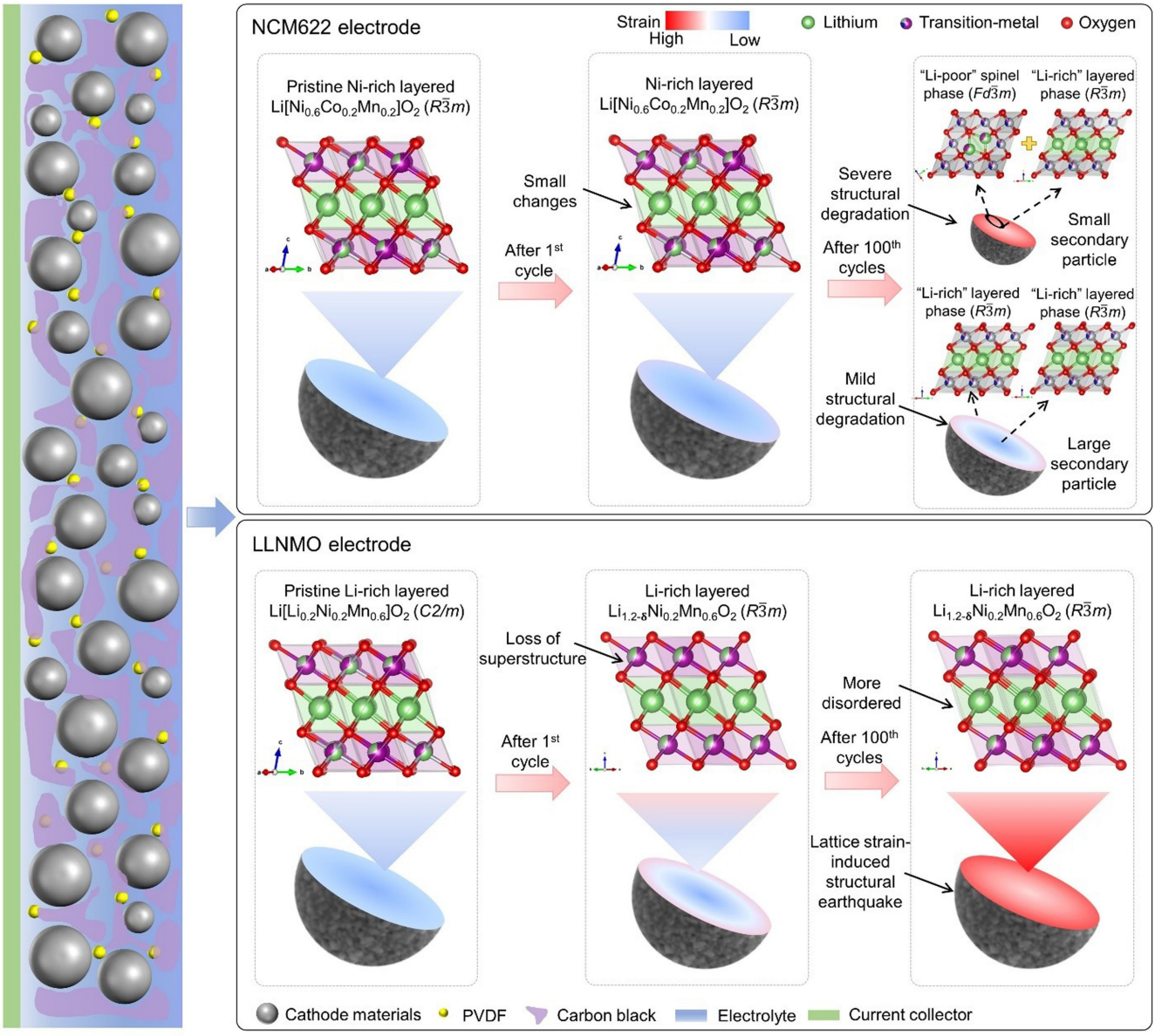

Figure 6. Schematic illustration of the progressive structural deterioration in NCM622 and LLNMO cathodes, illustrating the heterogeneous degradation occurring within the particles over extended cycling.

oxide with a layered/spinel/rock-salt-type heterostructure (LNMO-LSR). This was confirmed by the electrochemical features (Supplementary Figure S23–S24) and SXRD patterns (Figure S25). The weight fractions of monoclinic layered, cubic spinel, and rock-salt-type phases are found to be approximately 46, 42 and 12 %, respectively (Supporting Information Table S3). To visualize the spatial distribution of layered, spinel, and rock-salt-type phases in the LNMO-LSR, we conducted tomographic scanning of 12 slices using μ-XRD. The resulting μ-XRD tomographic reconstructions for the 12 slices with the step size of 1 μm are presented in Figure S26. Figure S26c showcases the averaged μ-XRD pattern of LNMO-LSR specifically for slice 1, which exhibits precise correspondence with its high-resolution SXRD pattern (Supplementary Figure S25). Figures S26d–g illustrate the μ-XRD tomographic reconstructions, and Figure S26h–k display the corresponding 2D μ-XRF reconstructions. It's apparent that these three phases predominantly coexist within the particles. Some particles exhibit a combination of spinel and layered phases with minimal content of the rock-salt-type phase. An unsupervised clustering algorithm was employed to analyze the μ-XRD imaging data of LMNO-LSR, illustrated in Figure S27b. In Region 1, the blue regions highlight the distribution of layered (*C2/m*) and spinel ($Fd\bar{3}m$) phases, closely mirroring the phase distribution depicted in Figure S27a. Figure S27c displays the corresponding XRD patterns for lines 1 and 2. The orange curve represents the distribution of l layered (*C2/m*) and spinel ($Fd\bar{3}m$) phases, while the blue curve exhibits features of layered (*C2/m*), spinel ($Fd\bar{3}m$), and rock-salt-type ($Fm\bar{3}m$) phases. These findings offer compelling evidence of the phase distribution's inhomogeneity within LMNO-LSR particles. Moreover, Ni and Mn elements demonstrate a uniform distribution within LNMO-LSR particles at the micrometer level, as evidenced by 2D μ-XRF maps (refer to Supplementary Figure S26h–k). Given the beam spot size used was approximately 1 μm^2 in cross-section, the disparity in crystalline and chemical composition is expected to be more pronounced in LNMO-LSR.

Conclusion

Overall, this work combines μXRD tomography with other advanced techniques to provide a comprehensive picture of microstructure and microstrain in the layered cathode materials for LIBs. These results could open new perspectives in the material synthesis and electrode manufacture, one promising application involves incorporating controlled hierarchical structures and gradients into the electrode materials.

Supporting Information

Experimental sections, description of data processing for μ-XRD and μ-XRF scanning tomography, 2D μ-XRD images, 2D μ-XRF images, SXRD patterns, and crystallographic parameters of the samples.

Author Contribution

W.H. conceived the idea and discussed with B.S., Y. Y., Z.W., C.H. S., M.K., H.E., S.I., X.G. and X.O.; W.H. and J.C. carried out the preparation experiments; D.F.S. performed the synchrotron-based μ-XRD and μ-XRF measurements; A.S. performed the NPD measurements; the tomography data analyzed by J.C.; W.H. wrote the preliminary draft with input D.F.S., S.I. and X.G.; all authors revised the manuscript and have given the approval to the final version of the manuscript.

Acknowledgements

This work was financially supported by the National Natural Science Foundation of China (Grant No. 22108218, 20A20145), Distinguished Young Foundation of Sichuan Province (Grant No. 2020JDJQ0027), and Sichuan Province Science and Technology Achievement Transfer and Transformation Project (Grant No. 21ZHSF0111). W. H. acknowledges "Young Talent Support Plan" of Xi'an Jiaotong University (HG6J016) and Qinchuangyuan Innovative Talent Project (QCYRCXM-2022-137). Our research work has gained benefit from beamtime allocation at BL04-MSPD and NL22-CLAESS at ALBA Synchrotron, Barcelona, Spain. We acknowledge the Paul Scherrer Institut, Villigen, Switzerland for provision of synchrotron radiation beamtime at beamline microXAS of the SLS. We acknowledge DESY (Hamburg, Germany), a member of the Helmholtz Association HGF, for the provision of experimental facilities. The authors wish to thank facility support of the 4B9A beamline of Beijing Synchrotron Radiation Facility (BSRF). We also thank the Instrument Analysis Center of Xi'an Jiaotong University for the assistance test. This work contributes to the research performed at CELEST (Center for Electrochemical Energy Storage Ulm-Karlsruhe) and was supported by the German Research Foundation (DFG) under Project ID 390874152 (POLiS Cluster of Excellence). Open Access funding enabled and organized by Projekt DEAL.

Conflict of Interest

The authors declare no conflict of interest.

Data Availability Statement

The data that support the findings of this study are available on request from the corresponding author. The data are not publicly available due to privacy or ethical restrictions.

Keywords: layered cathodes · reaction heterogeneity · local phase distribution · fatigue mechanism · μ-XRD tomography

[1] L. G. Wang, T. C. Liu, T. P. Wu, J. Lu, *Nature* **2022**, *611*(7934), 61–67.

[2] S. Q. Lu, Q. Zhang, F. Meng, Y. N. Liu, J. Mao, S. Guo, M. Y. Qi, Y. S. Xu, Y. Qiao, S. D. Zhang, K. Jiang, L. Gu, Y. Xia, S. Chen, G. Chen, A. M. Cao, L. J. Wan, *J. Am. Chem. Soc.* **2023**, *145*(13), 7397–7407.

[3] S. Tan, Z. Shadike, J. Li, X. Wang, Y. Yang, R. Lin, A. Cresce, J. Hu, A. Hunt, I. Waluyo, L. Ma, F. Monaco, P. Cloetens, J. Xiao, Y. Liu, X.-Q. Yang, K. Xu, E. Hu, *Nat. Energy* **2022**, *7*(6), 484–494.

[4] T. C. Liu, J. J. Liu, L. X. Li, L. Yu, J. C. Diao, T. Zhou, S. N. Li, A. Dai, W. G. Zhao, S. Y. Xu, Y. Ren, L. G. Wang, T. P. Wu, R. Qi, Y. G. Xiao, J. X. Zheng, W. Cha, R. Harder, I. Robinson, J. G. Wen, J. Lu, F. Pan, K. Amine, *Nature* **2022**, *606*(7913), 305–312.

[5] J. H. Min, L. M. Gubow, R. J. Hargrave, J. B. Siegel, Y. Y. Li, *Energy Environ. Sci.* **2023**, *16*(9), 3847–3859.

[6] K. Wang, W. Hua, X. Huang, D. Stenzel, J. Wang, Z. Ding, Y. Cui, Q. Wang, H. Ehrenberg, B. Breitung, C. Kubel, X. Mu, *Nat. Commun.* **2023**, *14*(1), 1487.

[7] J. Li, N. Sharma, Z. Jiang, Y. Yang, F. Monaco, Z. Xu, D. Hou, D. Ratner, P. Pianetta, P. Cloetens, F. Lin, K. Zhao, Y. Liu, *Science* **2022**, *376*(6592), 517–521.

[8] D. Chen, H. Tan, X. Rui, Q. Zhang, Y. Feng, H. Geng, C. Li, S. Huang, Y. Yu, *InfoMat* **2019**, *1*, 251–259.

[9] W. Hua, S. Wang, M. Knapp, S. J. Leake, A. Senyshyn, C. Richter, M. Yavuz, J. R. Binder, C. P. Grey, H. Ehrenberg, S. Indris, B. Schwarz, *Nat. Commun.* **2019**, *10*(1), 5365.

[10] W. Hua, J. Zhang, S. Wang, Y. Cheng, H. Li, J. Tseng, Z. Wu, C. H. Shen, O. Dolotko, H. Liu, S. F. Hung, W. Tang, M. Li, M. Knapp, H. Ehrenberg, S. Indris, X. Guo, *Angew. Chem. Int. Ed.* **2023**, *62*, e202214880.

[11] Z. Jing, S. Wang, Q. Fu, V. Baran, A. Tayal, N. P. M. Casati, A. Missyul, L. Simonelli, M. Knapp, F. Li, H. Ehrenberg, S. Indris, C. Shan, W. Hua, *Energy Storage Mater.* **2023**, *59*, 102775.

[12] S. Li, G. Qian, X. He, X. Huang, S. J. Lee, Z. Jiang, Y. Yang, W. N. Wang, D. Meng, C. Yu, J. S. Lee, Y. S. Chu, Z. F. Ma, P. Pianetta, J. Qiu, L. Li, K. Zhao, Y. Liu, *Nat. Commun.* **2022**, *13*(1), 704.

[13] C. Xu, K. Marker, J. Lee, A. Mahadevegowda, P. J. Reeves, S. J. Day, M. F. Groh, S. P. Emge, C. Ducati, B. Layla Mehdi, C. C. Tang, C. P. Grey, *Nat. Mater.* **2021**, *20*(1), 84–92.

[14] K. Y. Park, Y. Zhu, C. G. Torres-Castanedo, H. J. Jung, N. S. Luu, O. Kahvecioglu, Y. Yoo, J. T. Seo, J. R. Downing, H. D. Lim, M. J. Bedzyk, C. Wolverton, M. C. Hersam, *Adv. Mater.* **2022**, *34*(3), e2106402.

[15] X. H. Meng, T. Lin, H. Mao, J. L. Shi, H. Sheng, Y. G. Zou, M. Fan, K. Jiang, R. J. Xiao, D. Xiao, L. Gu, L. J. Wan, Y. G. Guo, *J. Am. Chem. Soc.* **2022**, *144*(25), 11338–11347.

[16] H. Yu, Y. Cao, L. Chen, Y. Hu, X. Duan, S. Dai, C. Li, H. Jiang, *Nat. Commun.* **2021**, *12*(1), 4564.

[17] Y. Bi, J. Tao, Y. Wu, L. Li, Y. Xu, E. Hu, B. Wu, J. Hu, C. Wang, J.-G. Zhang, Y. Qi, J. Xiao, *Science* **2020**, *370*(6522), 1313–1317.

[18] Q. Li, Z. Yao, E. Lee, Y. Xu, M. M. Thackeray, C. Wolverton, V. P. Dravid, J. Wu, *Nat. Commun.* **2019**, *10*(1), 1692.

[19] M. Chen, W. Hua, J. Xiao, J. Zhang, V. W. Lau, M. Park, G. H. Lee, S. Lee, W. Wang, J. Peng, L. Fang, L. Zhou, C. K. Chang, Y. Yamauchi, S. Chou, Y. M. Kang, *J. Am. Chem. Soc.* **2021**, *143*(43), 18091–18102.

[20] Z. S. Jiang, J. Z. Li, Y. Yang, L. Q. Mu, C. X. Wei, X. Q. Yu, P. Pianetta, K. J. Zhao, P. Cloetens, F. Lin, Y. J. Liu, *Nat. Commun.* **2020**, *11*(1), 2310.

[21] L. J. Chen, K. M. Song, J. Shi, J. Y. Zhang, L. W. Mi, W. H. Chen, C. T. Liu, C. Y. Shen, *Sci. China Mater.* **2021**, *64*(1), 105–114.

[22] W. B. Li, X. N. Guo, K. M. Song, J. C. Chen, J. Y. Zhang, G. C. Tang, C. T. Liu, W. H. Chen, C. Y. Shen, *Adv. Energy Mater.* **2023**, *13*(22), 2300648.

[23] L. de Biasi, B. Schwarz, T. Brezesinski, P. Hartmann, J. Janek, H. Ehrenberg, *Adv. Mater.* **2019**, *31*(26), e1900985.

[24] N. S. Luu, K.-Y. Park, M. C. Hersam, *Acc. Mater. Res.* **2022**, *3*, 511–524.

[25] H. Park, H. Park, K. Song, S. H. Song, S. Kang, K. H. Ko, D. Eum, Y. Jeon, J. Kim, W. M. Seong, H. Kim, J. Park, K. Kang, *Nat. Chem.* **2022**, *14*(6), 614–622.

[26] H. Cha, J. Kim, H. Lee, N. Kim, J. Hwang, J. Sung, M. Yoon, K. Kim, J. Cho, *Adv. Mater.* **2020**, *32*(39), 2003040.

[27] D. Petz, M. J. Muhlbauer, V. Baran, A. Schokel, V. Kochetov, M. Hofmann, V. Dyadkin, P. Staron, G. Vaughan, U. Lienert, P. Muller-Buschbaum, A. Senyshyn, *Energy Storage Mater.* **2021**, *41*, 546–553.

[28] J. Park, H. Zhao, S. D. Kang, K. Lim, C. C. Chen, Y. S. Yu, R. D. Braatz, D. A. Shapiro, J. Hong, M. F. Toney, M. Z. Bazant, W. C. Chueh, *Nat. Mater.* **2021**, *20*(7), 991–999.

[29] M. Ren, S. Zhao, S. N. Gao, T. Zhang, M. C. Hou, W. Zhang, K. Feng, J. Zhong, W. B. Hua, S. Indris, K. Zhang, J. Chen, F. J. Li, *J. Am. Chem. Soc.* **2022**. *145*, 224–233.

[30] G. Qian, J. Wang, H. Li, Z. F. Ma, P. Pianetta, L. Li, X. Yu, Y. Liu, *Natl. Sci. Rev.* **2022**, *9*(2), nwab146.

[31] Y. Yang, R. Xu, K. Zhang, S. J. Lee, L. Mu, P. Liu, C. K. Waters, S. Spence, Z. Xu, C. Wei, D. J. Kautz, Q. Yuan, Y. Dong, Y. S. Yu, X. Xiao, H. K. Lee, P. Pianetta, P. Cloetens, J. S. Lee, K. Zhao, F. Lin, Y. Liu, *Adv. Energy Mater.* **2019**, *9*(25), 1900674.

[32] G. Qian, J. Zhang, S.-Q. Chu, J. Li, K. Zhang, Q. Yuan, Z.-F. Ma, P. Pianetta, L. Li, K. Jung, Y. Liu, *ACS Energy Lett.* **2021**, *6*(2), 687–693.

[33] M. Ebner, F. Marone, M. Stampanoni, V. Wood, *Science* **2013**, *342*(6159), 716–720.

[34] V. Vanpeene, J. Villanova, A. King, B. Lestriez, E. Maire, L. Roué, *Adv. Energy Mater.* **2019**, *9*(18), 1803947.

[35] S. Müller, P. Pietsch, B. Brandt, P. Baade, V. De Andrade, F. De Carlo, V. Wood, *Nat. Commun.* **2018**, *9*, 2340.

[36] J. Wang, C. Eng, Y. C. Chen-Wiegart, J. Wang, *Nat. Commun.* **2015**, *6*, 7496.

[37] G. Sun, F. D. Yu, M. Lu, Q. J. Zhu, Y. S. Jiang, Y. Z. Mao, J. A. McLeod, J. Maley, J. Wang, J. G. Zhou, Z. B. Wang, *Nat. Commun.* **2022**, *13*(1), 6464.

[38] S. F. Lou, N. Sun, F. Zhang, Q. S. Liu, J. J. Wang, *Acc. Mater. Res.* **2021**, *2*(12), 1177–1189.

[39] Z. Jiang, J. Li, Y. Yang, L. Mu, C. Wei, X. Yu, P. Pianetta, K. Zhao, P. Cloetens, F. Lin, Y. Liu, *Nat. Commun.* **2020**, *11*(1), 2310.

[40] P. Bleuet, E. Welcomme, E. Dooryhee, J. Susini, J. L. Hodeau, P. Walter, *Nat. Mater.* **2008**, *7*(6), 468–472.

[41] D. Matras, A. Vamvakeros, S. D. M. Jacques, M. di Michiel, V. Middelkoop, I. Z. Ismagilov, E. V. Matus, V. V. Kuznetsov, R. J. Cernik, A. M. Beale, *J. Mater. Chem. A* **2021**, *9*(18), 11331–11346.

[42] A. Vamvakeros, D. Matras, S. D. M. Jacques, M. di Michiel, S. W. T. Price, P. Senecal, M. A. Aran, V. Middelkoop, G. B. G. Stenning, J. F. W. Mosselmans, I. Z. Ismagilov, A. M. Beale, *J. Catal.* **2020**, *386*, 39–52.

[43] P. Lu, P. F. Yan, E. Romero, E. D. Spoerke, J. G. Zhang, C. M. Wang, *Chem. Mater.* **2015**, *27*(4), 1375–1380.

[44] D. P. Finegan, A. Vamvakeros, C. Tan, T. M. M. Heenan, S. R. Daemi, N. Seitzman, M. Di Michiel, S. Jacques, A. M. Beale, D. J. L. Brett, P. R. Shearing, K. Smith, *Nat. Commun.* **2020**, *11*(1), 631.

[45] J. Chen, Y. Yang, Y. Tang, Y. Wang, H. Li, X. Xiao, S. Wang, M. S. D. Darma, M. Etter, A. Missyul, A. Tayal, M. Knapp, H.

Ehrenberg, S. Indris, W. Hua, *Adv. Funct. Mater.* **2023**, *33*, 2211515.
[46] W. Hua, K. Wang, M. Knapp, B. Schwarz, S. Wang, H. Liu, J. Lai, M. Müller, A. Schökel, A. Missyul, D. Ferreira Sanchez, X. Guo, J. R. Binder, J. Xiong, S. Indris, H. Ehrenberg, *Chem. Mater.* **2020**, *32*(12), 4984–4997.
[47] S. Wang, W. Hua, A. Missyul, M. S. D. Darma, A. Tayal, S. Indris, H. Ehrenberg, L. Liu, M. Knapp, *Adv. Funct. Mater.* **2021**, *31*(19), 2009949.
[48] S. Wang, T. Zhao, J. Chen, A. Missyul, L. Simonelli, L. Liu, F. Li, X. Kong, W. Hua, *ACS Appl. Mater. Interfaces* **2023**, *15*(16), 20200–20207.
[49] F. T. Geldasa, M. A. Kebede, M. W. Shura, F. G. Hone, *RSC Adv.* **2022**, *12*(10), 5891–5909.
[50] H. Zhou, F. X. Xin, B. Pei, M. S. Whittingham, *ACS Energy Lett.* **2019**, *4*(8), 1902–1906.
[51] S. Brandstetter, P. M. Derlet, S. Van Petegem, H. Van Swygenhoven, *Acta Mater.* **2008**, *56*(2), 165–176.
[52] K. Venkateswarlu, A. C. Bose, N. Rameshbabu, *Physica B+C* **2010**, *405*(20), 4256–4261.
[53] Y. Wu, C. Ma, J. H. Yang, Z. C. Li, L. F. Allard, C. D. Liang, M. F. Chi, *J. Mater. Chem. A* **2015**, *3*(10), 5385–5391.
[54] K. Ku, J. Hong, H. Kim, H. Park, W. M. Seong, S.-K. Jung, G. Yoon, K.-Y. Park, H. Kim, K. Kang, *Adv. Energy Mater.* **2018**, *8*(21), 1800606.
[55] X. Yang, S. Wang, D. Han, K. Wang, A. Tayal, V. Baran, A. Missyul, Q. Fu, J. Song, H. Ehrenberg, S. Indris, W. Hua, *Small* **2022**, *18*(25), e2201522.
[56] J. Zhang, Q. Zhang, D. Wong, N. Zhang, G. Ren, L. Gu, C. Schulz, L. He, Y. Yu, X. Liu, *Nat. Commun.* **2021**, *12*(1), 3071.
[57] W. He, W. Guo, H. Wu, L. Lin, Q. Liu, X. Han, Q. Xie, P. Liu, H. Zheng, L. Wang, X. Yu, D. L. Peng, *Adv. Mater.* **2021**, *33*(50), e2005937.

Manuscript received: February 14, 2024
Accepted manuscript online: May 3, 2024
Version of record online: June 17, 2024